Paleoceanography and Paleoclimatology

AGU100 ADVANCING EARTH AND SPACE SCIENCE

RESEARCH ARTICLE
10.1029/2019PA003625

Key Points:
- We present a new, isotope-enabled ensemble of CESM Last Millennium simulations
- Atlantic Multidecadal Oscillation and El Niño-Southern Oscillation variability influence isotopic patterns after eruptions
- Oxygen isotopic signatures can be used as a "fingerprint" for identifying the hemisphere in which past eruptions were located

Correspondence to:
S. Stevenson,
sstevenson@ucsb.edu

Citation:
Stevenson, S., Otto-Bliesner, B. L., Brady, E. C., Nusbaumer, J., Tabor, C., Tomas, R., et al. (2019). Volcanic eruption signatures in the isotope-enabled Last Millennium Ensemble. *Paleoceanography and Paleoclimatology*, *34*. https://doi.org/10.1029/2019PA003625

Received 8 APR 2019
Accepted 7 AUG 2019
Accepted article online 10 AUG 2019

Volcanic Eruption Signatures in the Isotope-Enabled Last Millennium Ensemble

S. Stevenson[1], B. L. Otto-Bliesner[2], E. C. Brady[2], J. Nusbaumer[3], C. Tabor[4], R. Tomas[2], D. C. Noone[5], and Z. Liu[6]

[1] Bren School of Environmental Science and Management, University of California, Santa Barbara, CA, USA, [2] Climate & Global Dynamics Laboratory, National Center for Atmospheric Research, Boulder, CO, USA, [3] NASA Goddard Institute for Space Studies and Center for Climate Systems Research, Columbia University, New York, NY, USA, [4] Department of Geosciences, University of Connecticut, Storrs, CT, USA, [5] College of Earth, Ocean and Atmospheric Sciences, Oregon State University, Corvallis, OR, USA, [6] Department of Geography, The Ohio State University, Columbus, OH, USA

Abstract Explosive volcanic eruptions are one of the largest natural climate perturbations, but few observational constraints exist on either the climate responses to eruptions or the properties (size, hemispheric aerosol distribution, etc.) of the eruptions themselves. Paleoclimate records are thus important sources of information on past eruptions, often through the measurement of oxygen isotopic ratios (δ^{18}O) in natural archives. However, since many processes affect δ^{18}O, the dynamical interpretation of these records can be quite complex. Here we present results from new, isotope-enabled members of the Community Earth System Model Last Millennium Ensemble, documenting eruption-induced δ^{18}O variations throughout the climate system. Eruptions create significant perturbations in the δ^{18}O of precipitation and soil moisture in central/eastern North America, via excitation of the Atlantic Multidecadal Oscillation. Monsoon Asia and Australia also exhibit strong precipitation and soil δ^{18}O anomalies; in these cases, δ^{18}O may reflect changes to El Niño-Southern Oscillation phase following eruptions. Salinity and seawater δ^{18}O patterns demonstrate the importance of both local hydrologic shifts and the phasing of the El Niño-Southern Oscillation response, both along the equator and in the subtropics. In all cases, the responses are highly sensitive to eruption latitude, which points to the utility of isotopic records in constraining aerosol distribution patterns associated with past eruptions. This is most effective using precipitation δ^{18}O; all Southern eruptions and the majority (66%) of Northern eruptions can be correctly identified. This work thus serves as a starting point for new, quantitative uses of isotopic records for understanding volcanic impacts on climate.

1. Introduction

Over the last millennium, explosive volcanism has been one of the strongest natural (nonanthropogenic) influences on the climate system. Volcanic eruptions inject sulfate aerosols into the stratosphere, which drastically reduce surface shortwave solar radiation and create global tropospheric cooling anomalies of several degrees or more (Robock, 2000). Events during the twentieth century, such as the 1991 eruption of Mt. Pinatubo, led to disruption of the global hydrological cycle (Trenberth & Dai, 2007); however, some preindustrial eruptions appear to have been orders of magnitude stronger, with accordingly larger destructive potential (Gao et al., 2008; Sigl et al., 2015). This highlights the importance of understanding the potential climatic impacts of future large eruptions (Bethke et al., 2017; Fasullo et al., 2017; Hopcroft et al., 2018; Zanchettin et al., 2016).

Climate model simulations indicate that the properties of a volcanic eruption strongly affect its climatic impacts. Important characteristics include eruption size (McGregor & Timmermann, 2011), latitude (Stevenson et al., 2016; Colose et al., 2016), season (Stevenson et al., 2017), and the initial state of the atmosphere and ocean (Pausata et al., 2015; Predybaylo et al., 2017). Yet before these simulated sensitivities can be used to inform risk assessments, they must be verified against observational benchmarks. Since so few eruptions have occurred during the modern observational era, this necessitates the use of paleoclimate information. Previous work has assessed eruption impacts primarily using tree ring archives; both the maximum latewood density (Briffa et al., 1998) and tree ring width data sets (Anchukaitis et al., 2010; Li et al., 2013) have been shown to record temperature and hydroclimate patterns associated with eruptions over the last millennium. Comparisons to date indicate substantial mismatches between simulated and reconstructed volcanic influences, yet the uncertainties associated with the input forcing data sets make it difficult to attribute these offsets definitively to either proxy limitations or model physical errors (Stevenson et al., 2016).

Paleoclimate proxies derived from the ratio of stable oxygen isotopes in water (hereafter δ^{18}O) are an additional and powerful set of tools. (Here δ is defined as $\delta = 1,000x(R/R_s - 1)$, where R is the ratio of ^{18}O to ^{16}O and R_s is the Vienna Standard Mean Ocean Water reference value.) δ^{18}O records are derived from a variety of sensors including ice cores (Jouzel et al., 1997), tree cellulose (Barbour et al., 2004; Roden et al., 2000), and speleothems (McDermott, 2004). There is thus a wealth of δ^{18}O information available, extending from the tropics to the high latitudes; additionally, many of these records have high (annual) resolution, making it possible for them to sense individual volcanic eruptions. However, to date, the use of δ^{18}O in the study of Last Millennium volcanism is quite limited. Previous work has made use of δ^{18}O information for creating large-scale reconstructions of land and ocean temperatures (Emile-Geay et al., 2013; Mann et al., 2009; Tierney et al., 2015); yet δ^{18}O proxies are known to be excellent recorders of changes in atmospheric circulation and hydrologic processes (Konecky et al., 2014; Noone & Simmonds, 2002; Vuille et al., 2003), meaning that they could potentially yield important independent constraints on volcanic climate impacts.

A complete understanding of how δ^{18}O proxy signals are generated is key to improving their quantitative use. Proxy records are often associated with uncertainties in seasonality, magnitude, dating, and other factors that can mask the climate response (Anchukaitis et al., 2010; Stevenson et al., 2013, 2017). Additionally, proxies do not directly record climate but rather the impact of climate on the variable of interest (e.g., tree ring width and precipitation isotopic ratios; Dee et al., 2015; Evans et al., 2013). Each of these sensors is affected by a different balance of physical (climatic) processes within the hydrological cycle, making it quite complex to use them to correctly infer past climate variations.

To address the need for dynamical understanding of δ^{18}O, "isotope-enabled" climate models have been developed, which are capable of directly simulating the variations in oxygen and hydrogen isotopic ratios throughout the hydrological cycle (Brady et al., 2019; Joussaume & Jouzel, 1993; Jouzel et al., 1987; Field et al., 2014; Noone & Simmonds, 2002; Noone & Sturm, 2010; Risi et al., 2010; Tindall et al., 2009). These models have demonstrated the large variations in processes affecting δ^{18}O in atmospheric, oceanic, and terrestrial contexts (Konecky et al., 2013; Russon et al., 2013; Wong et al., 2017). However, very few such models currently exist, and their use in studies of Last Millennium volcanism is still relatively uncommon (although some examples exist; e.g., Colose et al., 2016; Kobayashi et al., 2017). Studies of volcanic isotopic expression are further limited by the small number of available simulations covering the last millennium. The need for large ensembles to robustly detect volcanic forcing has been well demonstrated in previous studies (Fasullo et al., 2017; Otto-Bliesner et al., 2016; Stevenson et al., 2016), but to date, very few ensembles of isotope-enabled climate models exist.

The isotope-enabled version of the Community Earth System Model version 1 (CESM1) has recently become available (Brady et al., 2019). The CESM well simulates the climate of the twentieth century (Knutti et al., 2013) and has been used extensively to simulate the last millennium. The recently completed CESM Last Millennium Ensemble (LME; Otto-Bliesner et al., 2016) is a major advance in Last Millennium simulation, providing over 30 realizations of the 850–2005 period with all relevant forcings considered both collectively and individually. Using the new, isotope-enabled CESM code base (hereafter iCESM), additional LME members including δ^{18}O and δD fields have been created. These simulations are publicly available, as is the case for other LME members.

Here we present the simulated δ^{18}O responses to Last Millennium volcanism in the atmosphere, land, cryosphere, and ocean. By characterizing the global δ^{18}O response (sections 3–5), we can move toward improving δ^{18}O-based constraints on eruption properties (section 6).

2. Experimental Setup

All simulations analyzed here are Last Millennium simulations using iCESM1 (Brady et al., 2019). This uses a code base differing only slightly from that used to create the CESM LME (Otto-Bliesner et al., 2016), and the simulations presented here have been run over the same time period (850–2005) with forcings corresponding to the LME configuration (Brady et al., 2019). This means that when nonisotopic fields are being analyzed, the iLME simulations function as additional members of the LME as a whole.

Table 1
Simulations Completed to Date as Part of the Isotope-Enabled Last Millennium Ensemble

Ensemble	Size
Full forcing	3
Volcano only	2
Orbital only	1
Solar only	1
Greenhouse gas only	1

Note. All simulations cover the 850–2005 period.

As was done for the LME, the new, isotope-enabled simulations (hereafter "iLME") also include members run with only a single forcing agent (e.g., solar irradiance changes, greenhouse gas emissions, volcanic eruptions, and orbital changes) for use in attribution studies. The iLME members presently available are summarized in Table 1, although we anticipate the ensemble size to increase in the future; here we analyze the three full-forcing and two volcano-only simulations. Since the largest tropical eruptions occurred prior to 1850 and post-1850 anthropogenic influences may complicate detection of the volcanic signature, we restrict the analysis period here to 850–1850 (consistent with Stevenson et al., 2016). Volcanic aerosol forcing is implemented following the same protocol applied for the LME: Average monthly aerosol loadings in the nine latitudinal bands provided by the Gao et al. (2008) forcing data set are interpolated onto the three atmospheric layers closest to the climatological location of the base of the stratosphere.

For identification of volcanic responses, we follow the approach used in previous work (Stevenson et al., 2016). Eruptions with a peak aerosol mass mixing ratio greater than 10^{-8} in the Gao et al. (2008) data set are considered and classified according to their ratio of aerosols distributed in the Northern and Southern Hemispheres. As in Stevenson et al. (2016), eruptions with Northern/Southern Hemisphere aerosol ratios above 1.3 or below 0.7 are considered "Northern" (1176, 1213, 1600, 1641, 1762, and 1835) or "Southern" (1275, 1341, and 1452), respectively; the remainder are classified as "Tropical" (1258, 1284, 1809, and 1815). Note that as in the LME, the 1783 historical eruption of Laki occurs in 1762 in the model; the date of this event was assigned incorrectly in Gao et al. (2008). For all events, the eruption year is referred to as "Year 0" in subsequent analyses, such that for the April 1815 eruption of Mt. Tambora, "DJF +1" is made up of December 1815, January and February 1816, and so on. Anomalies are computed relative to the 850–1850 mean, to minimize the possibility of "preconditioning" of the preeruption baseline by other eruptions.

3. Atmospheric Response to Eruptions

The atmospheric response to eruptions is shown in Figures 1 and 2 using precipitation amount and surface air temperature, respectively. The precipitation amount signatures for Tropical and Northern eruptions reveal an equatorward migration of the Intertropical Convergence Zone (ITCZ) which is particularly pronounced during the boreal winter of the year following the eruption (DJF +1–2; Figures 1c and 1f). This is consistent with previous work showing that the ITCZ migrates away from the hemisphere with the largest volcanic aerosol loading (Colose et al., 2016; Pausata et al., 2015; Stevenson et al., 2016). The migration of the ITCZ is also tightly coupled with the tendency for El Niño initiation to become more common during the winter of DJF +1–2 (Figure 3; Stevenson et al., 2016). Other notable responses to Tropical and Northern eruptions include an overall reduction in Asian monsoon rainfall for the two boreal summers following the event (Figures 1b and 1e) and an increase in winter rainfall in western North America (Figures 1a, 1c, 1d, and 1f). These features are also influenced by the El Niño teleconnection pattern, as well as being part of the "El Niño-like" direct hydroclimate response to aerosol forcing previously documented in CESM (Stevenson et al., 2016).

Many of the temperature responses in Figures 1 and 2 have also been documented in Stevenson et al. (2016). These include an overall cooling of land masses, particularly in the Northern Hemisphere, and a tendency toward equatorial Pacific warming, which is the strongest during DJF +1–2 and following Northern/Tropical eruptions (Figures 2c and 2f). Cooling over land in the polar regions appears strongly dependent on eruption latitude; the Arctic and most of the Northern Hemisphere high latitudes cool much more strongly

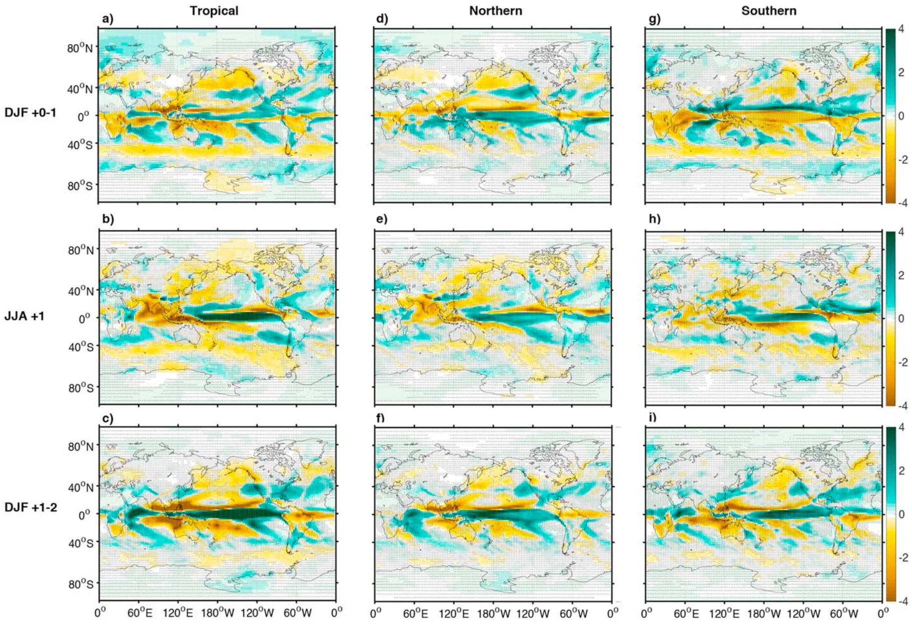

Figure 1. Anomalies in precipitation (mm/day) composited over the 2 years following Tropical (a–c), Northern (d–f), and Southern (g–i) eruptions. Stippling indicates values which are insignificant at 90% using a Wilcoxon rank-sum test. Top row (a,d,g) shows composites for DJF +0-1; middle row (b,e,h), for JJA +1; and bottom row (c,f,i), for DJF +1-2.

in response to Northern eruptions, consistent with the strong hemispheric differentials in aerosol loading. Likewise, Antarctica cools much more following Southern eruptions. In both polar regions, Tropical eruptions cause the strongest cooling, since these events have generally tended to be larger over the last millennium (Stevenson et al., 2016).

There are other features of interest in the high latitudes: for instance, the strong warming over Eurasia (Figure 2c). This has been previously attributed to a strengthening of the stratospheric polar vortex and associated positive phase of the North Atlantic Oscillation, bringing warmer air from the North Atlantic

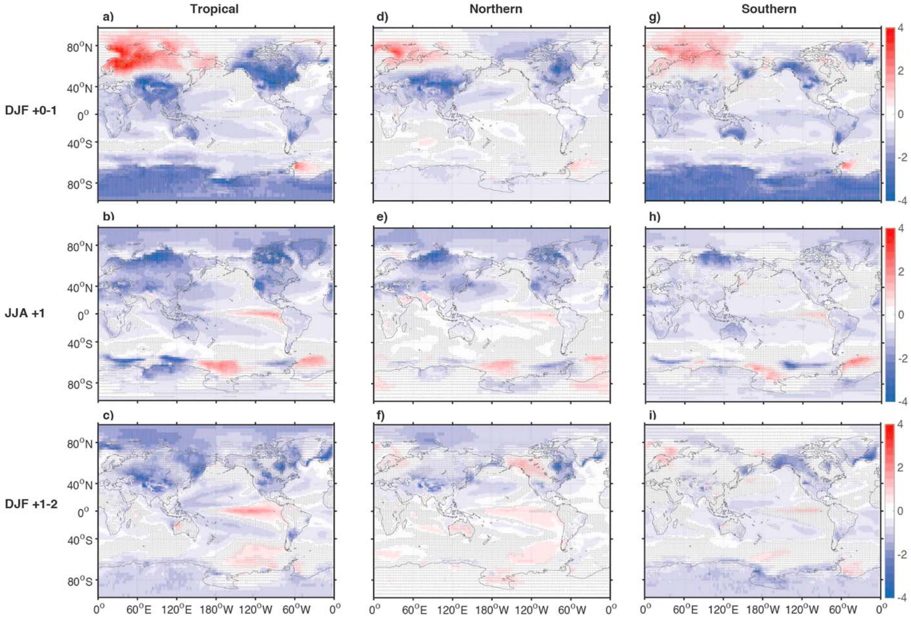

Figure 2. Anomalies in temperature (°C) composited over the 2 years following Tropical (a–c), Northern (d–f), and Souther (g–i) eruptions. Stippling indicates values which are insignificant at 90% using a Wilcoxon rank-sum test. Top row (a,d,g) shows composites for DJF +0-1; middle row (b,e,h), for JJA +1; and bottom row (c,f,i), for DJF +1-2.

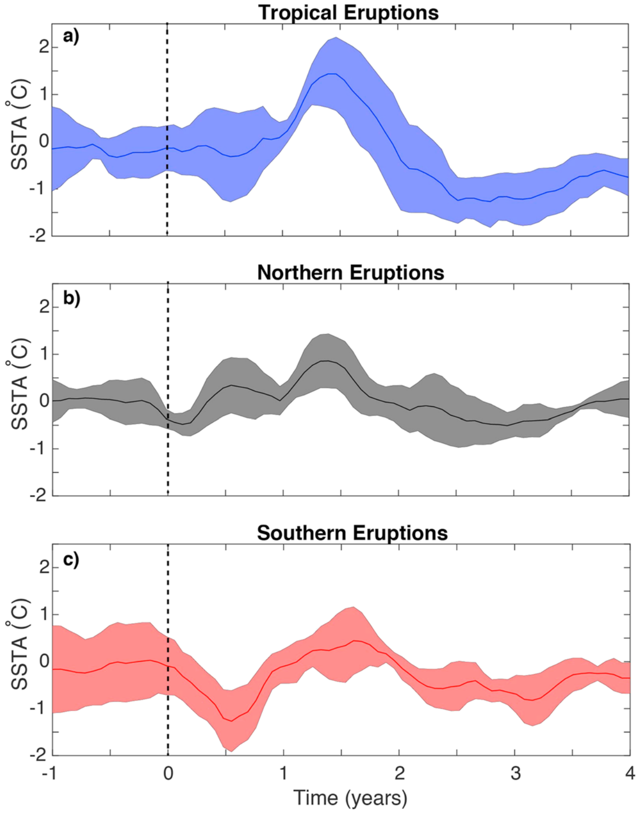

Figure 3. NINO3.4 SSTA following hemispherically stratified eruptions: a) Tropical, b) Northern, and c) Southern. Shading indicates ensemble max/min range and solid line the ensemble median.

(Perlwitz & Graf, 1995; Robock, 2000; Robock & Mao, 1992; Zambri & Robock, 2016). This mechanism has recently been called into question owing to the importance of internal variability (Polvani et al., 2019); we have not isolated the mechanism for this warming in CESM, but note that it is a statistically robust feature of CESM climate. This may be due to the larger magnitude of Last Millennium eruptions relative to Pinatubo; the response appears notably stronger than that noted in Polvani et al. (2019) for the larger Tropical eruptions.

Changes in the pattern of total precipitable water in response to eruptions have not generally been examined in previous work, but are shown in Figure 4. This quantity is tightly coupled with both patterns of convergence/divergence and background SST, and is here included as a demonstration of the impact of aerosol-driven cooling on the hydrological cycle. The dependence on eruption latitude is obvious: For Northern and Southern eruptions, the reduction in moisture is restricted almost entirely to the dominant hemisphere within the post-eruption year (Figures 4d and 4g), whereas the total precipitable water changes are much more symmetric for Tropical eruptions (Figure 4a). These asymmetries are moderated during subsequent years, as the aerosol loading (and associated shortwave cooling) propagates across hemispheres and delayed circulation responses become more dominant.

The structure of precipitation δ^{18}O ($\delta^{18}O_p$) responses to eruptions (Figure 5) reflects influences both from precipitation amount and temperature, but the balance of these influences varies strongly from region to region. In the tropics, the importance of the so-called "amount effect" is well documented (Dansgaard, 1964; Risi et al., 2008; Vuille et al., 2003), and indeed, regions with more depleted (negative) $\delta^{18}O_p$ values generally also exhibit increases in precipitation amount. This is particularly apparent over the equatorial oceans, where shifts in the convergence zones are most important. In the polar regions, the temperature dependence is much more dominant—there are notable enriched (positive) $\delta^{18}O_p$ anomalies over warm regions in Eurasia and depleted anomalies over Antarctica and the portions of Greenland/North America which experience the strongest cooling (Figure 5). As was the case for temperature in Figure 2, the $\delta^{18}O_p$ signatures depend strongly on eruption latitude, with Antarctic anomalies during DJF +0–1 largest after Tropical/Southern

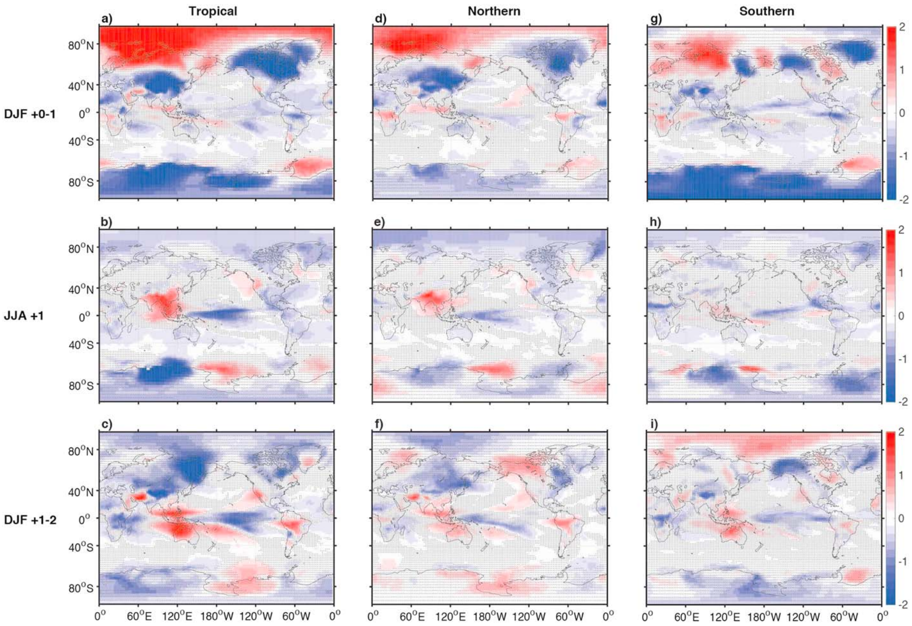

Figure 4. Anomalies in total precipitable water (colors) and 850-hPa winds (vectors) for the 2 years following Tropical (a–c), Northern (d–f), and Southern (g–i) eruptions Top row (a,d,g) shows composites for DJF +0-1; middle row (b,e,h), for JJA +1; and bottom row (c,f,i), for DJF +1-2.

eruptions (Figures 5a and 5g) and the Eurasian enrichment signal strongest following Tropical/Northern events (Figures 5a and 5d). Interestingly, the $\delta^{18}O_p$ depletion over Greenland/North America does not seem to correspond precisely to temperature, as the largest cooling occurs over the North American landmass yet $\delta^{18}O_p$ depletion is centered farther east (Figure 5a). This may indicate a role for changes to moisture source pathways in generating $\delta^{18}O_p$ anomalies, such as a shift in the average surface evaporation conditions, or in the amount of upstream rainout.

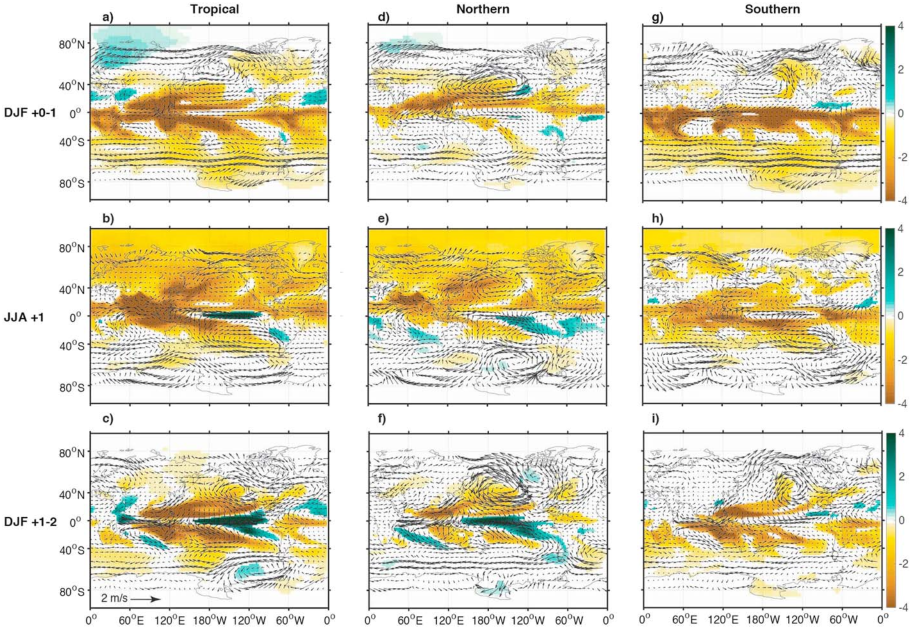

Figure 5. Anomalies in precipitation $\delta^{18}O$ (‰) for the 2 years following Tropical (a–c), Northern (d–f), and Southern (g–i) eruptions. Stippling indicates values which are insignificant at 90% using a Wilcoxon rank-sum test. Top row (a,d,g) shows composites for DJF +0-1; middle row (b,e,h), for JJA +1; and bottom row (c,f,i), for DJF +1-2.

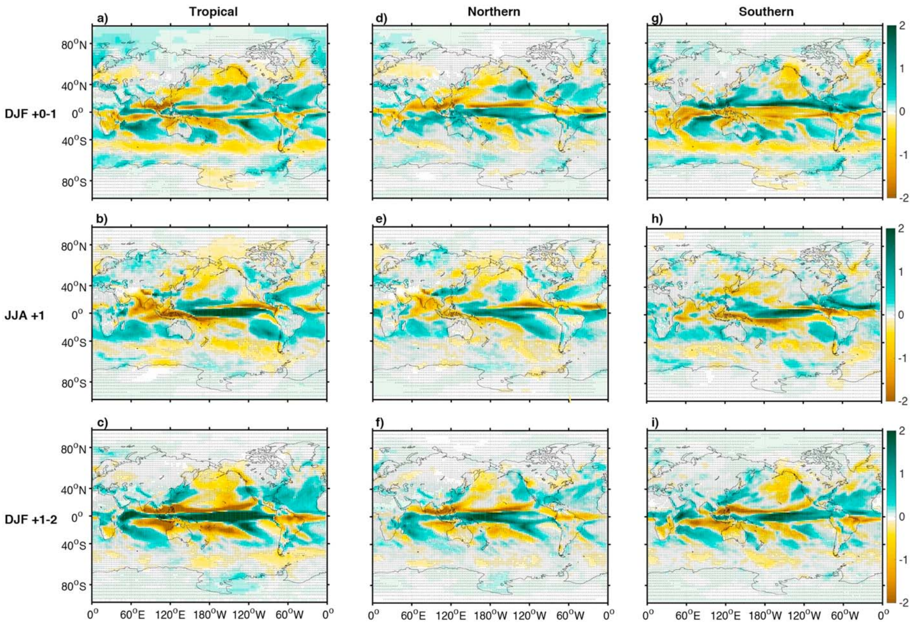

Figure 6. Anomalies in P-E (mm/day), for the 2 years following Tropical (a–c), Northern (d–f), and Southern (g–i) eruptions. Stippling indicates values which are insignificant at 90% using a Wilcoxon rank-sum test. Top row (a,d,g) shows composites for DJF +0-1; middle row (b,e,h), for JJA +1; and bottom row (c,f,i), for DJF +1-2;

During DJF +1–2, particularly following Tropical eruptions, the anomalies in $\delta^{18}O_p$ are quite large over the entire Australian continent (Figure 5c). Precipitation amount does not show correspondingly large anomalies, however (Figure 2c). We hypothesize that the increase in $\delta^{18}O_p$ could result from reduced precipitation and isotopic distillation upstream (Figures 4c, 4g, and 4k) or from a change in the moisture source over Australia. These mechanisms are consistent with the significant enrichment in column-integrated vapor $\delta^{18}O$ in the region (Figures 7c and 7g). The precipitation reduction in the northwestern Australian monsoon region is also rather large, extending over the Indian Ocean; this is likely related to El Niño initiation, as the El Niño teleconnection is quite strong in this area.

The $\delta^{18}O_p$ response in monsoon Asia is quite interesting as well. $\delta^{18}O_p$ enrichment is observed throughout the region, with relatively large anomalies over Thailand/Vietnam extending down to the equator. This pattern contrasts with precipitation amount, in which the reduction is strongest over the Himalayas and Indonesia (Figure 2) for JJA +1 following Tropical/Northern eruptions. However, it corresponds with a decrease in total precipitable water and the climatological surface convergence in the eastern Indian Ocean (Figure 4), in addition to a strong increase in vapor $\delta^{18}O$ which persists throughout the Asian subcontinent. We hypothesize that the increase in vapor $\delta^{18}O$ (and thus $\delta^{18}O_p$) is driven by the strong aerosol-driven cooling of the land surface (Figure 2; Stevenson et al., 2016), which suppresses evaporative flux into the atmosphere and therefore impacts $\delta^{18}O$ through modification of the degree of evaporative fractionation. This is borne out by the increase in the $\delta^{18}O$ of evapotranspiration flux in the region, seen in Figure 10. The reduction in the overall monsoon strength may also play a role, through an enhancement in transport of local moisture (Tabor et al., 2018).

Following eruptions of all latitude classes, a strong negative signal in $\delta^{18}O_p$ exists throughout the central/eastern portion of North America and over much of the Atlantic. This signature begins during the post-eruption year (JJA +1; Figures 5b, 5e, and 5h) and persists throughout the following boreal winter (Figures 5c, 5f, and 5i). During these same periods, however, the precipitation anomalies are close to zero throughout this region. This indicates that in this region, $\delta^{18}O_p$ may provide an additional degree of freedom with which to constrain changes in atmospheric circulation, even when the change in total precipitation amount is small. The changes to $\delta^{18}O_p$ are a result of coherent changes to large-scale circulation, as is apparent from the 850-hPa wind maps in Figure 4. These circulation changes are likely linked with the previously documented influence of eruptions on the Atlantic Multidecadal Oscillation (AMO; Otto-Bliesner et al., 2016). Strong volcanically induced cooling in the North Atlantic tends to drive a negative anomaly in

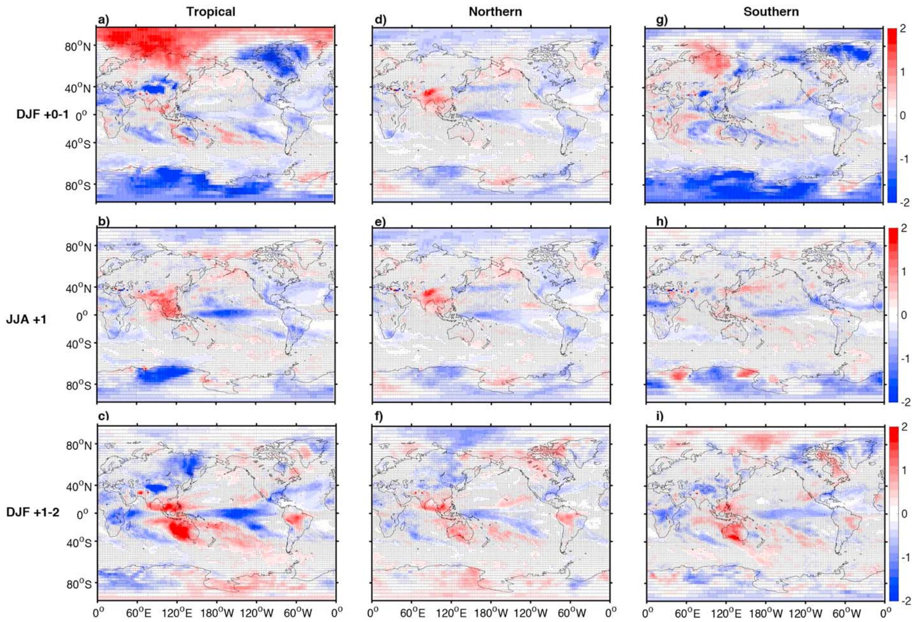

Figure 7. Anomalies in vapor δ^{18}O averaged over the entire vertical column, for the 2 years following Tropical (a–c), Northern (d–f), and Southern (g–i) eruptions. Stippling indicates values which are insignificant at 90% using a Wilcoxon rank-sum test. Top row (a,d,g) shows composites for DJF +0-1; middle row (b,e,h), for JJA +1; and bottom row (c,f,i), for DJF +1-2.

the AMO during the decade following the event. The North Atlantic cooling, in turn, creates reductions in overall evaporation from the ocean surface (see the overall positive values of North Atlantic precipitation - evaporation, or P-E, anomalies in Figure 6), explaining the lower δ^{18}O values observed in both precipitation and vapor (Figure 7). As was the case for monsoon Asia, the $\delta^{18}O_p$ anomalies appear strongest for Tropical and Northern eruptions, particularly within the year immediately after the event (Figures 5b, 5c, 5f, and 5g). We do anticipate that post-eruption El Niño initiation is playing a role in generating these circulation anomalies, as eastern Pacific warming is known to influence circulation in the Atlantic (Liu et al., 2004). Unfortunately, the available number of iLME members is not large enough to allow quantification of the El Niño role in generating these anomalies (as in Stevenson et al., 2016).

We note that inter-model differences do appear to alter post-eruption isotopic patterns; Last Millennium volcanic perturbations to precipitation $\delta^{18}O_p$ in the GISS ModelE (Colose et al., 2016) appear somewhat different from our results. The $\delta^{18}O_p$ pattern appears more El Niño-like following tropical eruptions in CESM, and the enrichment in the high latitudes is much stronger than in ModelE. Identifying all sources of inter-model differences are beyond the scope of the present analysis, but we note that the behavior of the El Niño-Southern Oscillation (ENSO) differs substantially across these models (Bellenger et al., 2014) as do the high-latitude dynamical responses (Colose et al., 2016). We anticipate that the regional patterns of $\delta^{18}O_p$ following eruptions will be sensitive to model physics, as is the case for other physical variables.

4. Terrestrial Response to Eruptions

The patterns of terrestrial hydroclimate responses to eruptions in the iLME track previous studies using CESM (Stevenson et al., 2016, 2017). Following Northern and Tropical eruptions, the previously documented JJA drying over monsoon Asia and DJF wetting over western North America may be seen (Figures 8b, 8d, 8f, and 8h). Wetting in the Amazon, the Caribbean, and Europe also occurs during JJA after Tropical eruptions (Figures 8b and 8d). These patterns are consistent with the regional signatures of temperature and precipitation amount in Figure 2.

Southern eruptions create a wetting in the northern Amazon/Caribbean that persists throughout the 2 years following the eruption, a much more robust signature than that seen for other eruption classes (Figure 8). This appears to relate to the persistent southwesterly wind anomaly in the region (Figure 4), which enhances

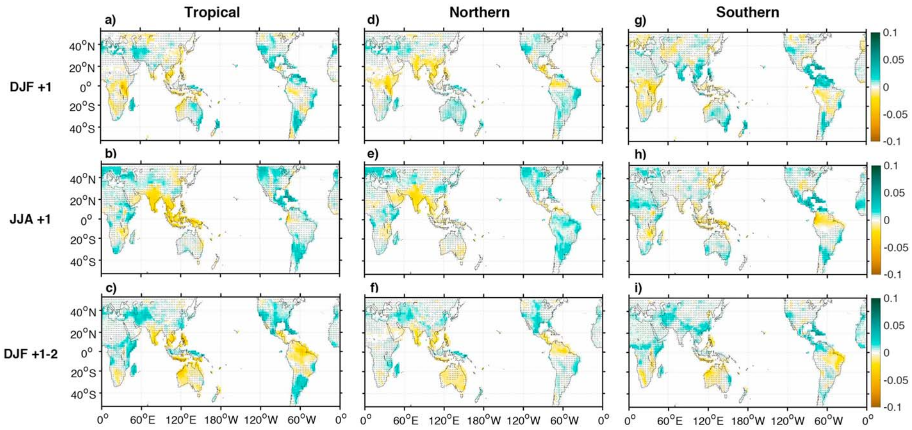

Figure 8. The 0- to 30-cm soil moisture for the 2 years following Tropical (a–c), Northern (d–f), and Southern (g–i) eruptions. Stippling indicates values which are insignificant at 90% using a Wilcoxon rank-sum test. Top row (a,d,g) shows composites for DJF +0-1; middle row (b,e,h), for JJA +1; and bottom row (c,f,i), for DJF +1-2.

moisture transport over Central America and the Caribbean. The shift may relate to the tendency for northward migration of the ITCZ following Southern eruptions (Stevenson et al., 2016). It is also possible that changes to Atlantic temperatures play a role; the North Atlantic cooling is much weaker following Southern eruptions relative to the responses to Northern and Tropical events. This should also favor a more northerly location of the ITCZ following Southern eruptions. Although previous work has demonstrated the importance of El Niño-driven warming to Amazon wetting via North Atlantic teleconnections (Liu et al., 2004), the relatively weak El Niño response after Southern eruptions (particularly during DJF 0–1) suggests that this is unlikely to be the dominant mechanism.

Anomalies in the δ^{18}O of 0- to 30-cm soil water are shown in Figure 9; this represents the layer most likely to influence δ^{18}O of tree cellulose in paleoclimate proxy reconstructions (Roden et al., 2000; Kanner et al., 2014). For comparison, anomalies in soil moisture over the same depths are shown in Figure 8. The patterns are broadly similar, as was the case for precipitation/temperature and $\delta^{18}O_p$. However, there are interesting discrepancies in many regions, suggesting a role for more complex influences from terrestrial processes.

Consistent with the amount effect, enriched soil δ^{18}O values appear over monsoon Asia in JJA +1 after Northern/Tropical eruptions, where overall precipitation is reduced (Figure 9b). Elsewhere, soil δ^{18}O seems much less coupled with the amount of soil moisture; for instance, the depletion in central/eastern U.S. soil δ^{18}O in the year following Northern/Tropical eruptions (Figure 9a–9c and 9d–9f) appears largely in the absence of corresponding soil moisture anomalies. As was the case for δ^{18}Opn, this seems to result from

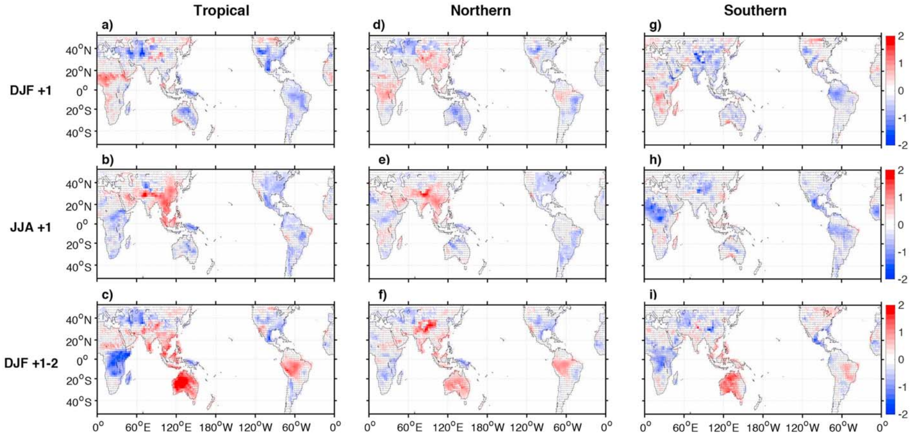

Figure 9. The 0- to 30-cm soil δ^{18}O for the 2 years following Tropical (a–c), Northern (d–f), and Southern (g–i) eruptions. Stippling indicates values which are insignificant at 90% using a Wilcoxon rank-sum test. Top row (a,d,g) shows composites for DJF +0-1; middle row (b,e,h), for JJA +1; and bottom row (c,f,i), for DJF +1-2.

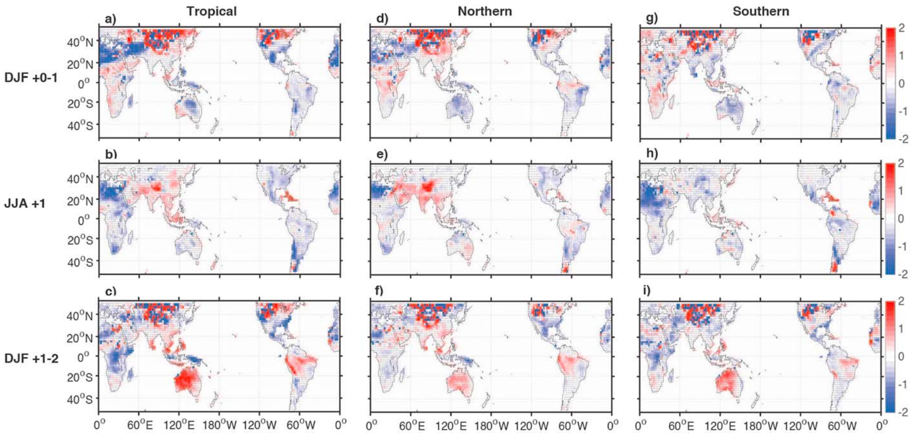

Figure 10. δ^{18}O of evapotranspiration flux for the 2 years following Tropical (a–c), Northern (d–f), and Souther (g–i) eruptions. Stippling indicates values which are insignificant at 90% using a Wilcoxon rank-sum test. Top row (a,d,g) shows composites for DJF +0-1; middle row (b,e,h), for JJA +1; and bottom row (c,f,i), for DJF +1-2.

changes to the AMO. The cyclonic anomaly over the basin described in section 3 tends to create northeasterly flow into the eastern United States, transporting relatively depleted moisture into the region and creating the observed depletion in vapor δ^{18}O (Figure 7).

Australia once again holds dynamically intriguing isotopic signatures. Tropical eruptions create soil δ^{18}O anomalies over the entire Australian continent of nearly 3‰ during DJF +1–2 (Figure 9c), with little change in soil moisture (Figure 8c). This seems related to an overall drying of the atmosphere in the region and associated enrichment in vapor δ^{18}O (Figures 4 and 7). Since the locations of enrichment in soil and precipitation δ^{18}O are quite similar, we conclude that $\delta^{18}O_p$ anomaly accumulation in the upper soil layer is likely to be a dominant factor in soil δ^{18}O generation. As for $\delta^{18}O_p$, the ENSO response to eruptions seems to be driving much of the change in soil water isotopic balance. This is most likely in the Tropical eruption case (Figure 9c), where the soil δ^{18}O is clearly more enriched during DJF +1–2 than for the other eruption classes. Such differences are consistent with the known behavior of ENSO in this model: The tendency for El Niño initiation is strongest during DJF +1–2 after Tropical eruptions (Figure 3; Stevenson et al., 2016). Further, the El Niño teleconnection is known to create strong drying over Australia due to the weakening of the Walker circulation and eastward migration of deep tropical convection.

In the Amazon, a strong enrichment occurs during DJF +1–2 following both Northern and Tropical eruptions (Figures 9c and 9f). Although some drying during Tropical DJF +1–2 takes place (Figure 8c), the anomalies in soil moisture are clearly not spatially coincident with the soil δ^{18}O features. Once again, enrichment in column-integrated vapor δ^{18}O and reductions in total precipitable water appear to drive these features during DJF +1–2. However, it is also possible that interactions with vegetation or other terrestrial processes are responsible. One candidate may be moisture recycling over the Amazon; the high recycling rates in the region should tend to inhibit the dissipation of a soil moisture isotope anomaly. Completely evaluating these hypotheses is beyond the scope of the present study, but we note that the complexity of capturing isotopic vegetative processes is expected to be an important limitation for iLME-based metrics (Brady et al., 2019; Riley et al., 2002; Wong et al., 2017).

African soil δ^{18}O also has complex sensitivities to volcanism. Tropical eruptions generate strong depletion in soil δ^{18}O during DJF +1–2 (Figure 9c) with no associated soil moisture anomaly. The changes in total precipitable water and vapor δ^{18}O are also small; the total change in evapotranspiration is relatively small in this region (not pictured), but the isotopic composition of the evapotranspiration flux does appear to change significantly (Figure 10c). Isotopic depletion is also observable in both vapor and precipitation over these periods, which could correspond to increased precipitation upstream (e.g., in the Indian Ocean and along the East African coast) and which might contribute to the soil water changes in Central/Eastern Africa. We also note that Southern eruptions show distinctly different soil δ^{18}O behavior, most notably in JJA +1 where a depletion occurs over much of the Sahel and western Africa. This appears more directly related to increases in regional precipitation (Figure 5), possibly related to migration of the ITCZ.

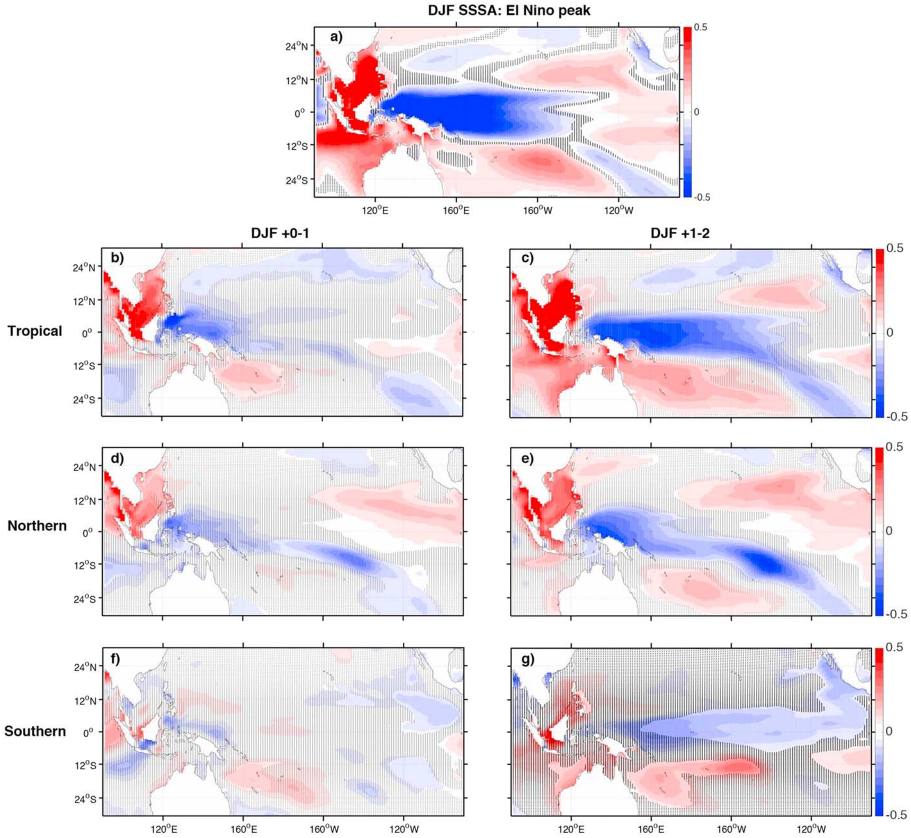

Figure 11. (a) Surface (upper model level; 0–5 m) salinity anomalies during DJF in which El Niños events peak. (b–g) Salinity anomalies during DJF, for the 2 years following eruptions. Stippling indicates regions where anomalies are statistically insignificant at 90%, using a rank-sum test. Left column (b,d,f) shows composites for DJF +0-1; right column (c,e,g), for DJF +1-2.

5. Oceanic Response to Eruptions

The tropical Pacific response to eruptions has been a topic of much previous research, particularly in the context of changes to the likelihood of El Niño initiation (Adams et al., 2003; Li et al., 2013; Mann et al., 2005). CESM has been previously shown to favor El Niño development during DJF +1–2 following strong eruptions (Stevenson et al., 2016), which is reproduced by the iLME (Figure 3). Tropical and Northern eruptions cause the strongest warming in the NINO3.4 index region (5°S–5°N, 190–240°E). Additionally, pronounced NINO3.4 cooling is observed for Southern events within the eruption year (Figure 3c). This tendency has also been previously documented and appears to result primarily from surface shortwave cooling (Stevenson et al., 2017) rather than constituting an enhancement in initiation of La Niña events via ocean dynamical processes.

The oceanic isotopic responses to volcanism are most relevant in the context of interpreting coral δ^{18}O records, derived from reefs on tropical islands. These are the most common source of high-resolution marine proxy data, particularly over the last millennium. Coral δ^{18}O is sensitive to SST via temperature-dependent fractionation during aragonite formation (Epstein et al., 1953) and also to the δ^{18}O of the surrounding seawater. This latter quantity is much less well studied, partially due to the extreme sparsity of observations (LeGrande & Schmidt, 2006). Seawater δ^{18}O is known to covary with salinity, since both are affected by the surface hydrologic balance and by ocean dynamical processes. As a result, seawater δ^{18}O is often used as a proxy for salinity, although the relationship between the two variables can sometimes be quite complex and temporally variable (Conroy et al., 2014; Stevenson et al., 2015, 2018). To date, the salinity and seawater δ^{18}O responses to volcanic eruptions have not been examined in detail, despite their crucial relevance for understanding coral proxy records.

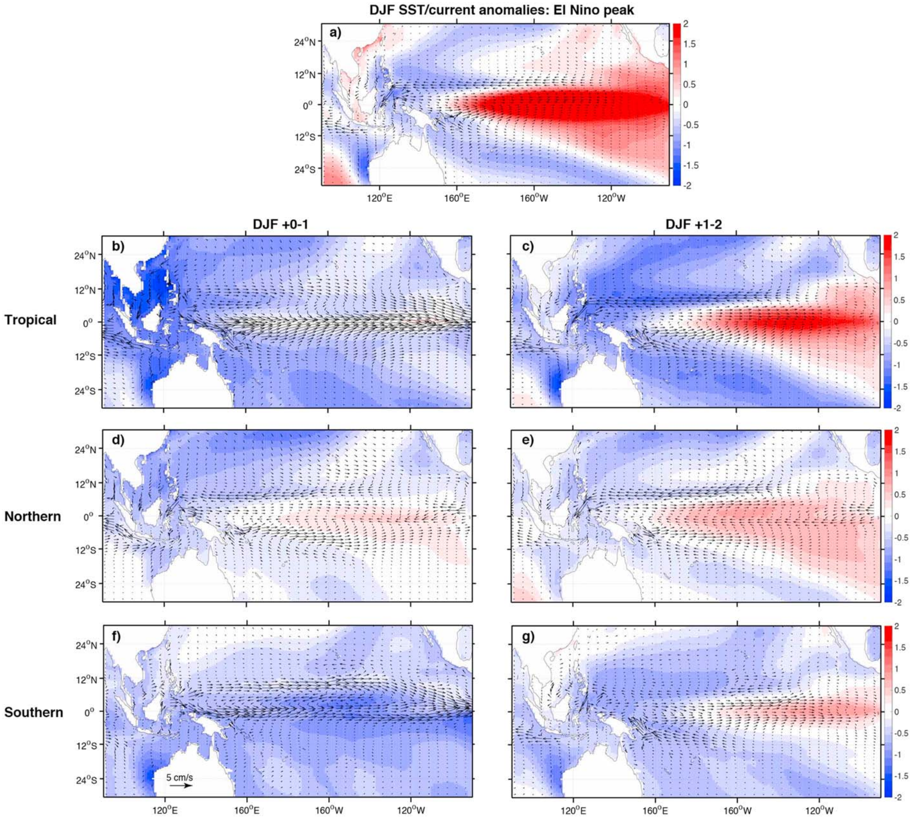

Figure 12. (a) Sea surface temperature (colors) and surface current velocity (arrows) anomalies during DJF in which El Niños events peak. (b–g) Sea surface temperature (colors) and surface current velocity (arrows) anomalies during DJF, for the 2 years following eruptions. As in Figure 11, the upper model layer is plotted (roughly upper 5 m).

The tropical Pacific salinity changes following eruptions in the iLME are shown in Figure 11. Analysis here is restricted to the surface ocean, as the majority of corals used for δ^{18}O record generation are found in the upper 15 m. There is a strong saltening tendency near Southeast Asia and the Philippines after Tropical and Northern eruptions, during both DJF +0–1 and DJF +1–2 (Figures 11b–11e). A strong fresh anomaly in the western Pacific exists in both cases as well. This anomaly extends much farther east following Tropical eruptions relative to Northern (Figures 11b and 11c vs. Figures 11d and 11e) and connects with a diagonally oriented fresh anomaly in the southeastern Pacific. The southeastern signal is associated with the migration of the South Pacific Convergence Zone (SPCZ), which moves eastward and equatorward in response to strong El Niño events (Widlansky et al., 2013). In contrast, relatively little salinity response exists in DJF 0–1 following Southern eruptions (Figure 11f). DJF +1–2 shows a significant, equatorially centered fresh anomaly, but the features of the DJF +1–2 Tropical/Northern response are largely absent (Figure 11g).

The salinity response to Tropical eruptions during DJF +1–2 corresponds closely with that seen at the peak of an El Niño event (Figure 11c vs. 11a). This is not the case for either Northern or Southern eruptions, despite the positive NINO3.4 SSTA values in both cases (Figure 3). This in turn suggests either a difference in the phasing of the ENSO response as a function of eruption latitude or a modification of the hydrological/dynamical structure of El Niño events in response to volcanic aerosol forcing. The present experimental setup is not capable of fully differentiating between these explanations, yet some qualitative inferences may be drawn.

Some evidence exists for the role of the changing temporal evolution of ENSO in influencing post-eruption salinity patterns. The El Niño peak following Northern/Tropical eruptions occurs slightly earlier than for Southern events (Figures 3a and 3b vs. Figure 3c), meaning that the El Niño has already begun to terminate during DJF +1–2. This termination, and the associated resumption of strong equatorial upwelling, likely explains the lack of freshening in the eastern equatorial Pacific (east of 140° W) in Tropical and Northern DJF +1–2, despite the relative enhancement of precipitation along the equator. Likewise, the SST anomalies are

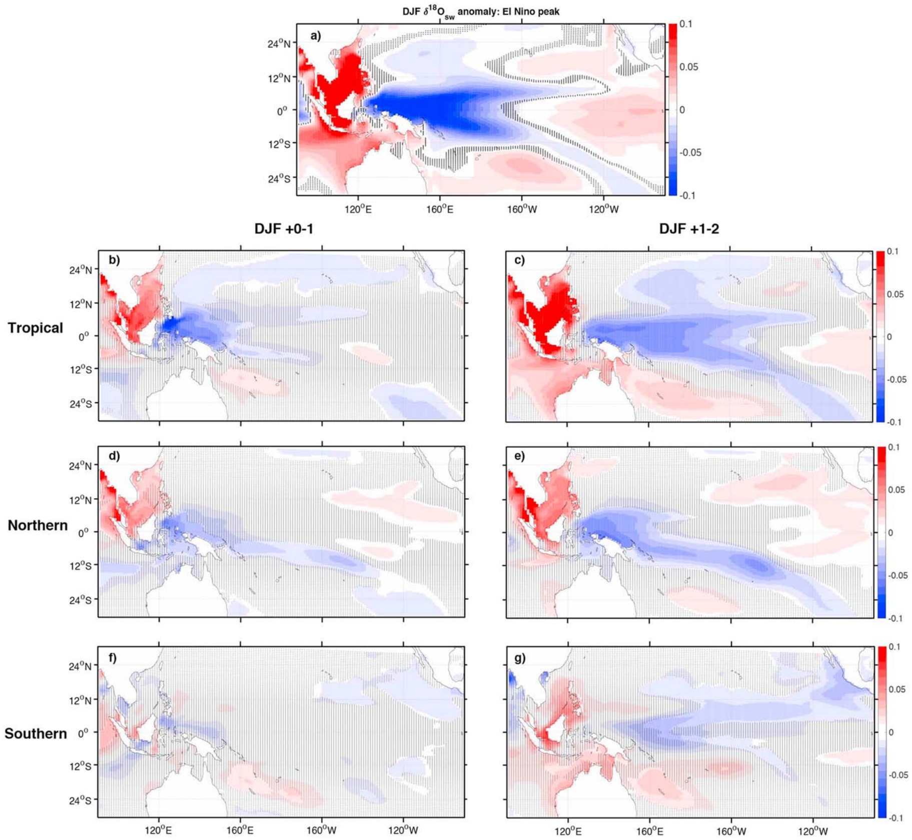

Figure 13. (a) Surface seawater $\delta^{18}O$ anomalies during DJF in which El Niños events peak. (b–g) Surface seawater $\delta^{18}O$ during DJF, for the 2 years following eruptions. Stippling indicates regions where anomalies are statistically insignificant at 90%, using a rank-sum test.

weaker during DJF +1–2 following Southern eruptions relative to the other two eruption classes, and there is a much larger eastward current anomaly in these cases (Figure 12g vs. Figure 12c and 12e). This indicates that the eastward transport of fresh water, begun during El Niño development, is still occurring during DJF +1–2 after Southern eruptions, whereas it has begun to terminate by this point after Northern/Tropical events (Figures 11c and 11e).

The hydrological influences on salinity are also quite strong and reflect a combination of ENSO evolution and direct forcing from aerosol shortwave forcing. The influence of local hydrology appears strongest in the western equatorial Pacific close to Southeast Asia, where El Niño-induced drying is strongest. This effect is largest for Tropical and Northern eruptions (Figures 11b–11e), whereas the drying in this region is nearly absent following Southern events (Figure 11g). Likewise, the influence of the ITCZ in the off-equatorial eastern Pacific can be seen most clearly for Tropical and Northern eruptions (Figures 11b–11e); saltening in the northern subtropical East Pacific is largest following Northern eruptions, consistent with the larger magnitude of ITCZ migration after these events (Stevenson et al., 2016).

Composites of seawater $\delta^{18}O$ ($\delta^{18}O_{sw}$) anomalies following volcanic eruptions in iCESM show patterns similar to salinity (Figure 13) in many locations. However, $\delta^{18}O_{sw}$ and salinity anomaly patterns are not identical. For instance, during DJF 0–1 in the off-equatorial Pacific following Tropical eruptions and the eastern Pacific following Northern eruptions, $\delta^{18}O_{sw}$ anomalies are proportionally smaller than salinity (Figures 11, 13a, and 13c). During DJF +1–2 after Tropical eruptions, $\delta^{18}O_{sw}$ anomalies north of the equator are enhanced relative to salinity (Figures 11 and 13b), and $\delta^{18}O_{sw}$ anomalies in the eastern Indian and southwestern Pacific are suppressed. The North Pacific $\delta^{18}O_{sw}$ anomalies seem to reflect the sensitivity of $\delta^{18}O_{sw}$ to changes in evaporation, as evidenced by the strong depletion signal in evaporative flux. The large negative anomalies in

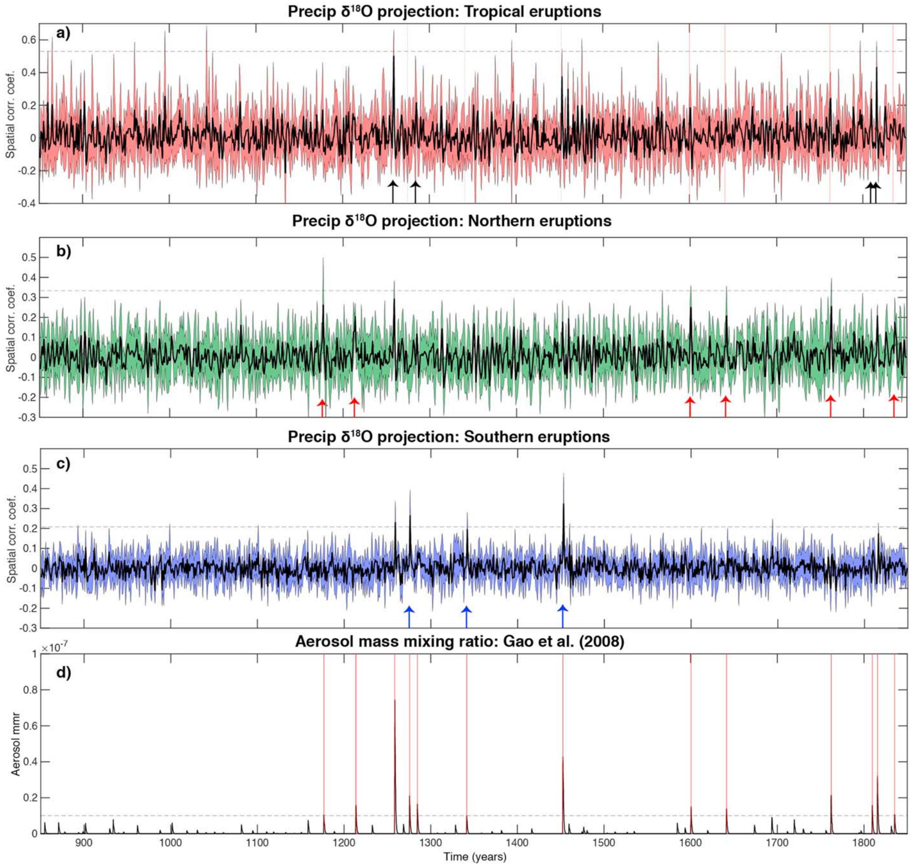

Figure 14. (a–c) Projection time series of precipitation δ^{18}O fields onto the composite anomalies associated with Tropical, Northern, and Southern eruption classes, respectively. Arrows indicate the occurrence years of the eruptions within the appropriate class. Solid black line indicates ensemble median; colored envelopes indicate the interquartile range. (d) Aerosol mass mixing ratio time series from the Gao et al. (2008) data set, used to force the Community Earth System Model new, isotope-enabled Last Millennium Ensemble simulations.

P-E in this region (Figure 6c) are also consistent with a dominance of evaporation at these latitudes in Tropical DJF +1–2. In the western Pacific, positive anomalies in seawater δ^{18}O seem to be driven by a combination of evaporative enrichment, and an enrichment in precipitation δ^{18}O.

6. Spatial Fingerprints of Eruption Latitude

In addition to describing the climatic response to volcanic eruptions, an understanding of the dynamics responsible for generating δ^{18}O anomalies can aid in the use of δ^{18}O records to reconstruct characteristics of past eruptions. This conceptual approach has previously been used to infer properties of eruptions in other contexts; for instance, Lavigne et al. (2013) concluded that the 1258 eruption of Mt. Samalas occurred in boreal summer based on the pattern of tephra deposits. In this case, the most obvious application is the identification of eruption hemisphere based on the spatial pattern of δ^{18}O, since many of the isotopic responses described above are strongly hemispherically dependent.

We have performed a spatial pattern correlation analysis, to infer the ability of $\delta^{18}O_p$ records to correctly identify the hemispheric structure of volcanic aerosol loading. The running DJF and JJA $\delta^{18}O_p$ anomaly fields are projected onto patterns of $\delta^{18}O_p$ anomaly during DJF +0–1, JJA +1, DJF +1–2, and JJA +2 seen in Figure 5 for each iLME ensemble member, yielding time series of pattern correlation values which vary according to the spatial structure of $\delta^{18}O_p$. Patterns having more similar spatiotemporal evolution to Figure 5 will thus yield higher correlation values; the results are seen in Figure 14. It is apparent that volcanic eruptions (as identified directly from the aerosol forcing time series; as in Stevenson et al., 2016) do indeed coincide with high pattern correlations, although there are many periods with high correlation which are not associated with major eruptions. This is an illustration of the large internal variability present in the climate system; the inclusion of additional iLME members in the computation would likely reduce the number of false positives in Figure 14. It is also important to note that $\delta^{18}O_p$ shows much more easily identifiable features in the pattern correlation time series than does the equivalent computation performed with precipitation amount (not pictured). $\delta^{18}O_p$ also yields a more effective eruption identification mechanism than soil $\delta^{18}O$; we hypothesize that this indicates the utility of high-latitude $\delta^{18}O$ signatures, which are not reflected in soil $\delta^{18}O$.

Figure 14 shows the pattern correlations derived from $\delta^{18}O_p$ patterns following Tropical, Northern, and Southern eruptions individually, along with the input aerosol forcing data set used during ensemble generation (Gao et al., 2008). It becomes clear that some eruptions project onto multiple $\delta^{18}O_p$ patterns, although this appears to occur only for the largest eruptions. For instance, after the 1258 Samalas eruption, correlations in all three patterns are significant at 99% (Figures 14a–14c). Tropical eruptions seem to be the least identifiable form of event, with only two eruptions detectable in Figure 14 and numerous noneruption years showing up as false positives. The reliability of this method seems to increase for higher-latitude eruptions; the noise level is much lower for the Northern eruption pattern, and the majority of events cross the 99% significance threshold (Figure 14b). However, Southern events have the highest signal-to-noise ratio of any of the eruption classes (Figure 14c); this may be due to the unique presence of negative $\delta^{18}O_p$ in Antarctica in the absence of strong high-latitude Northern Hemisphere values. Overall, Figure 14 suggests that the spatial structure of isotopic post-eruption signatures holds promise for improving reconstructions of eruption characteristics.

The ability of the projection method to identify the dominant eruption hemisphere is quantified by defining “success” as a projection time series significant at the 99% level for only the projection pattern associated with the eruption's actual type (according to the aerosol mass mixing ratio criterion of section 2). For the four Tropical eruptions, all are significant in the Tropical projection pattern (Figure 14a); yet the 1258 Samalas eruption also shows a significant spike in both the Northern and Southern projection patterns. The only “successfully identified” Tropical eruption is the 1815 Tambora event, and we conclude that the success rate of the method for Tropical eruptions is 25%. For the six Northern events, the rate is higher: The 1176, 1600, 1641, and 1762 events all have uniquely significant Northern patterns, and the success rate for these events is thus 66%. The three Southern events are most distinct; all three have patterns significant in the Southern projection time series and no others (although the 1452 Kuwae event shows up as marginally significant in the Tropical time series). The success rate for Southern eruptions can thus be considered nearly 100%.

7. Discussion and Conclusions

This study presents the first look at isotopic anomalies associated with large volcanic eruptions in the isotope-enabled CESM1 (Brady et al., 2019). Volcanic impacts on physical climate are similar to previous results using this version of the model (Stevenson et al., 2016, 2017). The hydroclimate signatures of tropical and high-latitude Northern Hemisphere eruptions bear a qualitative resemblance to El Niño teleconnection patterns. The difference in total precipitable water as a function of eruption hemisphere is quite striking and reflective of the temperature influence on the hydrological cycle; for Southern eruptions, the response is isolated nearly entirely to the Southern Hemisphere during the year following the eruption. The evolution of the ENSO system following eruptions differs as a function of hemisphere as well: NINO3.4 SSTA values are negative within the eruption year following Southern eruptions, a somewhat “La Niña-like” pattern which is known to differ dynamically from La Niña generation (Stevenson et al., 2017). After Tropical and Northern eruptions, the NINO3.4 SSTA is near zero within the eruption year, and during the boreal winter of the following year, eruptions of all three latitude classes show El Niño-like warming in the central equatorial Pacific (Stevenson et al., 2016; Figure 3).

Changes to $\delta^{18}O_p$ following volcanic eruptions are linked with changes in precipitation amount in many locations, consistent with the known importance of the amount effect (negative correlation between precipitation amount and $\delta^{18}O_p$; Galewsky et al., 2016). This is true primarily over the equatorial Pacific and portions of the Maritime Continent, especially for Tropical and Northern eruptions during JJA +1 and DJF +1–2 (Figure 5). The influence of temperature is much larger over the high latitudes, particularly over northern Canada/Greenland, Eurasia, and Antarctica. Strong cooling and negative $\delta^{18}O_p$ anomalies appear in Canada/Greenland and Antarctica following Tropical and Southern eruptions. In contrast, much of the

Arctic ocean and the northern part of Eurasia exhibits positive δ^{18}O anomalies in response to the "winter warming" pattern identified in previous studies (Perlwitz & Graf, 1995; Robock, 2000; Zambri & Robock, 2016).

In some locations, $\delta^{18}O_p$ anomalies are strong despite little change in local precipitation amount: Examples include the Indian subcontinent, much of Australia, and the Atlantic basin including the central/eastern United States. In Australia, $\delta^{18}O_p$ changes seem to be linked with either a change in the moisture source or a shift in upstream isotopic distillation. In monsoon Asia, the volcanically driven land surface cooling leads to a suppression of evaporative flux and related vapor depletion. However, the Atlantic anomalies are of particular note since they indicate a strong link between $\delta^{18}O_p$ and AMO changes, which appear to result from changes in evaporation over the North Atlantic and associated modification in vapor δ^{18}O transported into eastern North America. This effect is highly sensitive to the hemispheric structure of volcanic aerosol loading.

Terrestrial isotopic and hydroclimate patterns are strongly linked with atmospheric responses. The Atlantic circulation anomaly drives persistent increases to soil moisture in the Caribbean and northern Amazon, which is particularly strong following Southern eruptions. This circulation shift also creates depleted soil δ^{18}O over the central and eastern United States, most likely via changes to $\delta^{18}O_p$. Anomalies in African soil δ^{18}O are also quite large and independent of soil moisture changes. This seems to result from a combination of changes to the δ^{18}O of evapotranspiration and possibly from a change in upstream precipitation causing the observed changes in vapor and precipitation δ^{18}O. In Australia, soil δ^{18}O again shows a significant response to Tropical eruptions, related to drying of the atmosphere in response to El Niño initiation and corresponding increases in vapor δ^{18}O.

This study also shows the salinity responses to hemispherically stratified eruptions for the first time. Strong shifts in the location and extent of the SPCZ are observed after Northern and Tropical eruptions; the SPCZ shifts to the southeast within the eruption year, likely related to enhancement in El Niño initiation. Strong saltening occurs in the far western Pacific (near the Philippines) after both Northern and Tropical eruptions, relating to the tendency for El Niño-induced Walker circulation weakening and associated reduction in precipitation. The equatorial salinity structure differs across eruption classes, partly due to the slower development of El Niños during DJF +1–2 after Southern eruptions relative to Northern/Tropical. In the former case, freshening is present across the eastern half of the basin due to eastward advection of fresh water from the warm pool. In the latter, El Niños have already begun to terminate in DJF +1–2, which inhibits the propagation of eastward anomalies and favors the upwelling of more saline subsurface waters.

Seawater isotopic changes track salinity in many regions but are distinct from one another, particularly in off-equatorial locations. In the North Pacific, Northern/Tropical eruptions show strong evaporation-related seawater δ^{18}O shifts toward more enriched/depleted values, respectively. The saltening tendency near the Philippines is muted in δ^{18}O space, possibly due to compensation from changes in precipitation δ^{18}O or advective influences. Additionally, the eastern Pacific freshening following Southern eruptions is weaker in $\delta^{18}O_{sw}$, most likely due to a larger sensitivity of $\delta^{18}O_{sw}$ to vertical mixing relative to salinity (Stevenson et al., 2018).

These results are a first step toward using isotopic records as independent constraints on past eruption characteristics. Rather than treating δ^{18}O as another estimate of moisture balance, the iLME indicates that δ^{18}O records may be sensitive to large-scale dynamics in ways that hydroclimate alone is not. The most striking example is the influence of the AMO on precipitation and soil δ^{18}O in central and eastern North America. This allows characterization either of the AMO response to volcanism (in cases where the eruption latitude is previously known) or of the latitudinal structure itself, when previous information is absent. Likewise, the isotopic responses in monsoon Asia and Australia are robust and hemispherically dependent, making these additional candidate regions.

The capacity for quantitative reconstruction of hemispheric aerosol distribution using δ^{18}O information has been demonstrated using pattern correlation. By computing a running correlation with the anomaly patterns in precipitation δ^{18}O associated with eruptions in different latitude classes, we are able to recover time series strongly resembling the input aerosol forcing data set. This suggests that the precipitation δ^{18}O responses are a unique feature of the climate system, whose presence can be used to infer the dominant hemisphere of an eruption. It should be noted that not all patterns perform equally well; in particular, Tropical eruptions are not as easily identified, likely since they have features in common with both Northern and Southern eruptions. The identification of Southern eruptions is much more reliable, however, and we anticipate that future analyses will be able to advance these techniques even further. Overall, this work demonstrates that isotope-enabled models provide a unique opportunity to aid interpretation of δ^{18}O systematics in response to Last Millennium eruptions.

Acknowledgments
This work is supported by an NSF EaSM grant (AGS 1243125) to B. O.-B. S. S. was also supported by an NSF P2C2 grant (AGS 1805143). Z. L. is supported by NSF P2C2 (AGS 1810682). This material is based upon work supported by the National Center for Atmospheric Research, which is a major facility sponsored by the National Science Foundation under Cooperative Agreement 1852977. The CESM project is supported primarily by the National Science Foundation. Computing resources (doi:10.5065/D6RX99HX) were provided by the Climate Simulation Laboratory at NCAR's Computational and Information Systems Laboratory, sponsored by the National Science Foundation and other agencies.

References

Adams, J. B., Mann, M. E., & Ammann, C. M. (2003). Proxy evidence for an El Niño-like response to volcanic forcing. *Nature*, *426*, 274–278.

Anchukaitis, K. J., Buckley, B. M., Cook, E. R., Cook, B. I., D'Arrigo, R. D., & Ammann, C. M. (2010). Influence of volcanic eruptions on the climate of the Asian monsoon region. *Geophysical Research Letters*, *37*, L22703. https://doi.org/10.1029/2010GL044843

Barbour, M. M., Roden, J. S., Farquhar, G. D., & Ehleringer, J. R. (2004). Expressing leaf water and cellulose oxygen isotope ratios as enrichment above source water reveals evidence of a Peclet effect. *Oecologia*, *138*(3), 426–435. https://doi.org/10.1007/s00442-003-1449-3

Bellenger, H., Guilyardi, E., Leloup, J., Lengaigne, M., & Vialard, J. (2014). ENSO representation in climate models: From CMIP3 to CMIP5. *Climate Dynamics*, *42*, 1999–2018. https://doi.org/10.1007/s00382-013-1783-z

Bethke, I., Outten, S., Ottera, O. H., Hawkins, E., Wagner, S., Sigl, M., & Thorne, P. (2017). Potential volcanic impacts on future climate variability. *Nature Climate Change*, *7*, 799–805.

Brady, E., Stevenson, S., Bailey, D., Liu, Z., Noone, D., Nusbaumer, J., et al. (2019). The connected isotopic water cycle in the Community Earth System Model. *Journal of Advances in Modeling Earth Systems*. https://doi.org/10.1029/2019MS001663

Briffa, K. R., Jones, P. D., Schweingruber, F. H., & Osborn, T. J. (1998). Influence of volcanic eruptions on Northern Hemisphere summer temperature over the past 600 years. *Nature*, *393*, 450. https://doi.org/10.1038/30943

Colose, C. M., LeGrande, A. N., & Vuille, M. (2016). Hemispherically asymmetric volcanic forcing of tropical hydroclimate and water isotopologue variability during the last millennium. *Earth System Dynamics Discussions*, *7*, 681–696. https://doi.org/10.5194/esd-2016-19

Conroy, J. L., Cobb, K. M., Lynch-Stieglitz, J., & Polissar, P. J. (2014). Constraints on the salinity-oxygen isotope relationship in the central tropical Pacific Ocean. *Marine Chemistry*, *161*, 26–33. https://doi.org/10.1016/j.marchem.2014.02.001

Dansgaard, W. (1964). Stable isotopes in precipitation. *Tellus*, *16*, 436–468.

Dee, S., Emile-Geay, J., Evans, M. N., Allam, A., Steig, E. J., & Thompson, D. M. (2015). PRYSM: An open-source framework for PRoxY System Modeling, with applications to oxygen-isotope systems. *Journal of Advances in Modeling Earth Systems*, *7*, 1220–1247. https://doi.org/10.1002/2015MS000447

Emile-Geay, J., Cobb, K., Mann, M., & Wittenberg, A. T. (2013). Estimating tropical Pacific SST variability over the past millennium. Part 2: Reconstructions and uncertainties. *Journal of Climate*, *26*, 2329–2352. https://doi.org/10.1175/JCLI-D-11-00511

Epstein, S., Buchsbaum, R., Lowenstam, H. A., & Urey, H. C. (1953). Revised carbonate/water isotopic temperature scale. *Geological Society of America Bulletin*, *64*(11), 1315–1326. https://doi.org/10.1130/0016-7606(1953)64[1315:RCITS]2.0.CO;2

Evans, M. N., Tolwinski-Ward, S. E., Thompson, D. M., & Anchukaitis, K. J. (2013). Applications of proxy system modeling in high resolution paleoclimatology. *Quaternary Science Reviews*, *76*, 16–28.

Fasullo, J. T., Tomas, R., Stevenson, S., Otto-Bliesner, B., Brady, E., & Wahl, E. (2017). The amplifying influence of increased ocean stratification on a future year without a summer. *Nature Communications*, *8*, 1236. https://doi.org/10.1038/s41467-017-01302-z

Field, R. D., Kim, D., LeGrande, A. N., Worden, J., Kelley, M., & Schmidt, G. A. (2014). Evaluating climate model performance in the tropics with retrievals of water isotopic composition from Aura TES. *Geophysical Research Letters*, *41*, 6030–6036. https://doi.org/10.1002/2014GL060572

Galewsky, J., Steen-Larsen, H. C., Field, R. D., Worden, J., Risi, C., & Schneider, M. (2016). Stable isotopes in atmospheric water vapor and applications to the hydrologic cycle. *Reviews of Geophysics*, *54*, 809–865. https://doi.org/10.1002/2015RG000512

Gao, C. C., Robock, A., & Ammann, C. (2008). Volcanic forcing of climate over the past 1500 years: An improved ice core-based index for climate models. *Journal of Geophysical Research*, *113*, D23111. https://doi.org/10.1029/2008JD010239

Hopcroft, P. O., Kandlbauer, J., Valdes, P. J., & Sparks, R. S. J. (2018). Reduced cooling following future volcanic eruptions. *Climate Dynamics*, *51*(4), 1449–1463.

Joussaume, S., & Jouzel, J. (1993). Paleoclimatic tracers: An investigation using an atmospheric general circulation model under Ice Age conditions. 2: Water isotopes. *Journal of Geophysical Research*, *98*, 2807–2830.

Jouzel, J., Alley, R. B., Cuffey, K. M., Dansgaard, W., Grootes, P., Hoffmann, G., et al. (1997). Validity of the temperature reconstruction from water isotopes in ice cores. *Journal of Geophysical Research*, *102*, 26,471–26,487.

Jouzel, J., Russell, G. L., Suozzo, R. J., Koster, R. D., White, J. W. C., & Broecker, W. S. (1987). Simulations of the HDO and $H_2\ ^{18}O$ atmospheric cycles using the NASA GISS general circulation model: The seasonal cycle for present-day conditions. *Journal of Geophysical Research*, *92*, 14,739–14,760. https://doi.org/10.1029/JD092iD12p14739

Kanner, L., Buenning, N., Stott, L., Timmermann, A., & Noone, D. (2014). The role of soil processes in δ^{18}O terrestrial climate proxies. *Global Biogeochemical Cycles*, *28*, 239–252. https://doi.org/10.1002/2013GB004742

Knutti, R., Masson, D., & Gettelman, A. (2013). Climate model genealogy: Generation CMIP5 and how we got there. *Geophysical Research Letters*, *40*, 1194–1199. https://doi.org/10.1002/grl.50256

Kobayashi, T., Menviel, L., Jeltsch-Thömmes, A., Vinther, B. M., Box, J. E., Muscheler, R., et al. (2017). Volcanic influence on centennial to millennial Holocene Greenland temperature change. *Nature Scientific Reports*, *7*, 1441.

Konecky, B. L., Russell, J. M., Rodysill, J. R., Vuille, M., Bijaksana, S., & Huang, Y. (2013). Intensification of southwestern Indonesian rainfall over the past millennium. *Geophysical Research Letters*, *40*, 386–391. https://doi.org/10.1029/2012GL054331

Konecky, B., Russell, J., Vuille, M., & Rehfeld, K. (2014). The Indian Ocean Zonal Mode over the past millennium in observed and modeled precipitation isotopes. *Quaternary Science Reviews*, *103*, 1–18. http://doi.org/10.1016/j.quascirev.2014.08.019

Lavigne, F., Degeai, J.-P., Komorowski, J.-C., Guillet, S., Robert, V., Lahitte, P., et al. (2013). Source of the great A.D. 1257 mystery eruption unveiled, Samalas volcano, Rinjani Volcanic Complex, Indonesia. *Proceedings of the National Academy of Sciences*, *110*(42), 16,742–16,747.

LeGrande, A. N., & Schmidt, G. A. (2006). Global gridded data set of the oxygen isotopic composition in seawater. *Geophysical Research Letters*, *33*, L12604. https://doi.org/10.1029/2006GL026011

Li, J., Xie, S. P., Cook, E. R., Morales, M. S., Christie, D. A., Johnson, N. C., et al. (2013). El Niño modulations over the past seven centuries. *Nature Climate Change*, *3*, 822–826.

Liu, Z., Zhang, Q., & Wu, L. (2004). The remote impact on tropical Atlantic climate variability: The dynamic assessment and statistical assessment. *Journal of Climate*, *17*, 1529–1549.

Mann, M., Rutherford, S., Wahl, E., & Ammann, C. (2005). Testing the fidelity of methods used in proxy-based reconstructions of past climate. *Journal of Climate*, *18*, 4097–4107.

Mann, M. E., Zhang, Z., Rutherford, S., Bradley, R. S., Hughes, M., Shindell, D., et al. (2009). Global signatures and dynamical origins of the Little Ice Age and Medieval climate anomaly. *Science*, *326*, 1256–1260.

McDermott, F. (2004). Palaeo-climate reconstruction from stable isotope variations in speleothems: A review. *Quaternary Science Reviews*, *23*, 901–918.

McGregor, S., & Timmermann, A. (2011). The effect of explosive tropical volcanism on ENSO. *Journal of Climate*, *24*, 2178–2191.

Noone, D., & Simmonds, I. (2002). Associations between δ^{18}O of water and climate parameters in a simulation of atmospheric circulation for 1979–95. *Journal of Climate*, *15*, 3150–3169.

Noone, D., & Sturm, C. (2010). Comprehensive dynamical models of global and regional water isotope distributions. In J. B. West, G. J. Bowen, T. E. Dawson, & K. P. Tu (Eds.), *Isoscapes* pp. 195–219). Netherlands: Springer.

Otto-Bliesner, B., Brady, E. C., Fasullo, J., Jahn, A., Landrum, L., Stevenson, S., et al. (2016). Climate variability and change since 850 C.E.: An ensemble approach with the Community Earth System Model (CESM). *Bulletin of the American Meteorological Society*, *97*, 735–754. https://doi.org/10.1175/BAMS-D-14-00233.1

Pausata, F. S. R., Chafik, L., Caballero, R., & Battisti, D. S. (2015). Impacts of high-latitude volcanic eruptions on ENSO and AMOC. *Proceedings of the National Academy of Sciences*, *112*(45), 13,784–13,788.

Perlwitz, J., & Graf, H.-F. (1995). The statistical connection between tropospheric and stratospheric circulation of the Northern Hemisphere in winter. *Journal of Climate*, *8*, 2281–2295.

Polvani, L. M., Banerjee, A., & Schmidt, A. (2019). Northern Hemisphere continental winter warming following the 1991 Mt. Pinatubo eruption: Reconciling models and observations. *Atmospheric Chemistry and Physics*, *19*, 6351–6366. https://doi.org/10.5194/acp-19-6351-2019

Predybaylo, E., Stenchikov, G. L., Wittenberg, A. T., & Zeng, F. (2017). Impacts of a Pinatubo-size volcanic eruption on ENSO. *Journal of Geophysical Research: Atmospheres*, *122*, 925–947. https://doi.org/10.1002/2016JD025796

Riley, W. J., Still, C. J., Torn, M. S., & Berry, J. A. (2002). A mechanistic model of $H_2^{18}O$ and $C^{18}OO$ fluxes between ecosystems and the atmosphere: Model description and sensitivity analyses. *Global Biogeochemical Cycles*, *16*(4), 1095. https://doi.org/10.1029/2002GB001878

Risi, C., Bony, S., & Vimeux, F. (2008). Influence of convective processes on the isotopic composition (δ^{18}O and δ^{18}O δD) of precipitation and water vapor in the tropics: 2. Physical interpretation of the amount effect. *Journal Geophysical Research*, *113*, D19306. https://doi.org/10.1029/2008JD009943

Risi, C., Bony, S., Vimeux, F., & Jouzel, J. (2010). Water-stable isotopes in the LMDZ4 general circulation model: Model evaluation for present? Day and past climates and applications to climatic interpretations of tropical isotopic records. *Journal of Geophysical Research*, *115*, D12. https://doi.org/10.1029/2009JD013255

Robock, A. (2000). Volcanic eruptions and climate. *Reviews of Geophysics*, *38*(2), 191–219.

Robock, J., & Mao, J. (1992). Winter warming from large volcanic eruptions. *Geophysical Research Letter*, *19*, 2405–2408. https://doi.org/10.1029/92GL02627

Roden, J. S., Lin, G., & Ehleringer, J. R. (2000). A mechanistic model for interpretation of hydrogen and oxygen isotope ratios in tree-ring cellulose. *Geochimica et Cosmochimica Acta*, *64*(1), 21–35.

Russon, T., Tudhope, A. W., Hegerl, G. C., Collins, M., & Tindall, J. (2013). Inter-annual tropical Pacific climate variability in an isotope-enabled CGCM: Implications for interpreting coral stable oxygen isotope records of ENSO. *Climate of the Past*, *9*, 1543–1557.

Sigl, M., Winstrup, M., McConnell, J. R., Welten, K. C., Plunkett, G., Ludlow, F., et al. (2015). Timing and climate forcing of volcanic eruptions for the past 2,500 years. *Nature*, *523*, 543–549. https://doi.org/10.1038/nature14565

Stevenson, S., Fasullo, J. T., Otto-Bliesner, B. L., Tomas, R. A., & Gao, C. (2017). Role of eruption season in reconciling model and proxy responses to tropical volcanism. *Proceedings of the National Academy of Sciences*, *114*(8), 1822–1826. https://doi.org/10.1073/pnas.1612505114

Stevenson, S., McGregor, H. V., Phipps, S., & Fox-Kemper, B. (2013). Quantifying errors in coral-based ENSO estimates: Towards improved forward modeling of δ^{18}O. *Paleoceanography*, *28*, 633–649. https://doi.org/10.1002/palo.20059

Stevenson, S., Otto-Bliesner, B., Fasullo, J., & Brady, E. (2016). 'El Nino-like' hydroclimate responses to volcanic eruptions. *Journal of Climate*, *29*, 2907–2921.

Stevenson, S., Powell, B., Cobb, K., Nusbaumer, J., Merrifield, M., & Noone, D. (2018). Twentieth century seawater δ^{18}O dynamics and implications for coral-based climate reconstruction. *Paleoceanography and Paleoclimatology*, *33*, 606–625. https://doi.org/10.1029/2017PA003304

Stevenson, S., Powell, B., Merrifield, M., Cobb, K., Nusbaumer, J., & Noone, D. (2015). Characterizing seawater oxygen isotopic variability in a regional ocean modeling framework: Implications for coral proxy records. *Paleoceanography*, *30*, 1573–1593. https://doi.org/10.1002/2015PA002824

Tabor, C., Otto-Bliesner, B. L., Brady, E. C., Nusbaumer, J., Zhu, J., Erb, M. P., et al. (2018). The δ^{18}O response in the South Asian Monsoon to precession. *Journal of Geophysical Research: Atmospheres*, *123*, 5927–5946. https://doi.org/10.1029/2018JD028424

Tierney, J. E., Abram, N. J., Anchukaitis, K. J., Evans, M. N., Giry, C., Kilbourne, K. H., et al. (2015). Tropical sea surface temperatures for the past four centuries reconstructed from coral archives. *Paleoceanography*, *30*, 226–252. https://doi.org/10.1002/2014PA002717

Tindall, J. C., Valdes, P. J., & Sime, L. C. (2009). Stable water isotopes in HadCM3: Isotopic signature of El Niño-Southern Oscillation and the tropical amount effect. *Journal of Geophysical Research*, *114*, D04111. https://doi.org/10.1029/2008JD010825

Trenberth, K. E., & Dai, A. (2007). Effects of Mount Pinatubo volcanic eruption on the hydrological cycle as an analog of geoengineering. *Geophysical Research Letters*, *34*, L15702. https://doi.org/10.1029/2007GL030524

Vuille, M., Bradley, R. S., Werner, M., Healy, R., & Keimig, F. (2003). Modeling δ^{18}O in precipitation over the tropical Americas: 1. Interannual variability and climatic controls. *Journal Geophysical Research*, *108*(D6), 4174. https://doi.org/10.1029/2001JD002038

Widlansky, M., Timmermann, A., Stein, K., McGregor, S., Schneider, N., England, M., et al. (2013). Shifted South Pacific rainfall bands in a warming climate. *Nature Climate Change*, *3*, 417–423.

Wong, T., Nusbaumer, J., & Noone, D. C. (2017). Evaluation of modeled land-atmosphere exchanges with a comprehensive water isotope fractionation scheme in version 4 of the Community Land Model (CLM4). *Journal of Advances in Modeling Earth Systems*, *9*, 978–1001. https://doi.org/10.1002/2016MS000842

Zambri, B., & Robock, A. (2016). Winter warming and summer monsoon reduction after volcanic eruptions in Coupled Model Intercomparison Project 5 (CMIP5) simulations. *Geophysical Research Letters*, *43*, 10,920–10,928. https://doi.org/10.1002/2016GL070460

Zanchettin, D., Khodri, M., Timmreck, C., Toohey, M., Schmidt, A., Gerber, E. P., et al. (2016). The Model Intercomparison Project on the climatic response to Volcanic forcing (VolMIP): Experimental design and forcing input data for CMIP6. *Geoscientific Model Development*, *9*, 2701–2719.